J. Fluid Mech. (2004), *vol.* 498, *pp.* 139–159.
DOI: 10.1017/S0022112003006712 Printed in the United Kingdom

Numerical modelling for three-dimensional heat and fluid flow through a bank of cylinders in yaw

By A. NAKAYAMA, F. KUWAHARA AND T. HAYASHI

Department of Mechanical Engineering, Shizuoka University, 3-5-1 Johoku, Hamamatsu, 432-8561 Japan

(Received 9 December 2002 and in revised form 13 August 2003)

A numerical model for a three-dimensional heat and fluid flow through a bank of infinitely long cylinders in yaw has been proposed to investigate complex flow and heat transfer characteristics associated with manmade structures such as extended fins and plate fins in heat transfer equipment. By exploiting the periodicity of the structure, only one structural unit has been taken as a calculation domain. An economical quasi-three-dimensional calculation procedure has been proposed to replace exhaustive full three-dimensional numerical manipulations. It has been shown that, under macroscopically uniform flow, the three-dimensional governing equations reduce to quasi-three-dimensional forms, in which all derivatives associated with the axis of the cylinder can be either eliminated or replaced by other determinable expressions. Thus, only two-dimensional storage is required for the dependent variables in question. Extensive numerical calculations were carried out for various sets of the porosity, degree of anisotropy, Reynolds number and macroscopic flow direction in a three-dimensional space. The numerical results thus obtained for periodically fully developed flow and temperature fields were integrated over a structural unit to determine the permeability tensor, Forchheimer tensor and directional interfacial heat transfer coefficient, to elucidate the effects of yaw angle on these macroscopic flow and heat transfer characteristics. Upon examining these numerical data, a useful set of explicit expressions has been established for the permeability tensor, Forchheimer tensor and directional interfacial heat transfer coefficient to characterize flow and heat transfer through a bank of cylinders in yaw.

1. Introduction

A number of workers, including Grimson (1937, 1938), Omohundro, Bergelin & Colburn (1949), Bergelin *et al.* (1950), Bergelin, Brown & Doberstein (1952) and Zukauskas (1987), have carried out extensive experimental investigations for heat transfer from a bundle of tubes in crossflow, and provided useful experimental data and correlations for designing crossflow heat exchangers. In designing such heat exchangers, the correlations for the pressure drop and interfacial heat transfer coefficient, as functions of the macroscopic velocity vector (i.e. its magnitude and direction in reference to the axis of the tube) and other structural parameters, are required.

Detailed flow and temperature fields within a heat exchanger assembly may be investigated by numerically solving the set of governing equations based on first principles, so as to resolve all scales of flow and heat transfer in the system. However, in reality, it would be impossible to resolve such details, even with the most powerful super-computer available today. A grid system, designed for a comparatively

large-scale heat exchanger system, would not be fine enough to describe the details of flow and heat transfer around a fin in a heat transfer element. Thus, heat exchangers are usually designed following semi-empirical procedures based on simple heat-balance relationships and analytical models designed for possible heat transfer elements, as comprehensively reviewed by Shah & London (1978) and Kays & London (1984).

Since the initiative attempts made by Hubbert (1956), Slattery (1967) and Whitaker (1967) to derive macroscopic laws from microscopic principles of fluid dynamics, considerable efforts have been directed towards establishing general macroscopic equations for flows in porous media. This concept of local volume-averaging theory (VAT), widely used in the study of porous media (e.g. Cheng 1978; Vafai & Tien 1981; Quintard & Whitaker 1993; Nakayama 1995) may be exploited to investigate the flow and heat transfer within complex heat and fluid flow equipment consisting of small-scale elements, such as a bundle of tubes and fins, which we do not want to represent by a grid. For example, the hot and cold fluid passages in a compact heat exchanger can be treated as two distinct porous media with highly anisotropic permeabilities. Also, we need a certain macroscopic model for estimating the pressure drop, when we perform Computational fluid dynamics (CFD) calculations of engine nacelles to account for bundles of hydraulic tubes, ribs and some other obstructions (DesJardin, personal communication 2001). There are a number of other situations in which we have to introduce macroscopic models to describe complex flow and heat transfer systems.

Nakayama & Kuwahara (1999) derived a set of macroscopic governing equations for turbulent heat and fluid flow through an isotropic porous medium in local thermal equilibrium, while the set of governing equations based on the two-energy equation model for laminar flow through a non-thermal equilibrium isotropic porous medium was obtained by Nakayama, Kuwahara & Xu (2001), by integrating the microscopic governing equations, namely, the continuity equation, the Navier–Stokes equation and the energy equation. We can use these macroscopic equations to investigate the flow and heat transfer within complex equipment consisting of small-scale elements. According to Nakayama *et al.* (2001, 2002*a*), the set of macroscopic equations based on the volume-averaging theory for the case of laminar flow through an anisotropic porous medium is

$$\frac{\partial \langle u_j \rangle^f}{\partial x_j} = 0, \tag{1}$$

$$\rho_f \left(\frac{\partial \langle u_i \rangle^f}{\partial t} + \frac{\partial}{\partial x_j} \langle u_j \rangle^f \langle u_i \rangle^f \right) = -\frac{\partial \langle p \rangle^f}{\partial x_i} + \frac{\partial}{\partial x_j} \left[\mu_f \left(\frac{\partial \langle u_i \rangle^f}{\partial x_j} + \frac{\partial \langle u_j \rangle^f}{\partial x_i} \right) \right] - \phi \left(\mu_f K_{f_{ij}}^{-1} + \phi_f \rho_f b_{f_{ij}} \left(\langle u_k \rangle^f \langle u_k \rangle^f \right)^{1/2} \right) \langle u_j \rangle^f, \tag{2}$$

$$\rho_f c_{p_f} \left(\frac{\partial \langle T \rangle^f}{\partial t} + \frac{\partial}{\partial x_j} \langle u_j \rangle^f \langle T \rangle^f \right) = \frac{\partial}{\partial x_j} \left[k_f \frac{\partial \langle T \rangle^f}{\partial x_j} + \frac{1}{V_f} \int_{A_{int}} k_f T n_j \, \mathrm{d}A - \rho_f c_{pf} \langle u_j' T' \rangle^f \right] + h_f a_f (\langle T \rangle^s - \langle T \rangle^f), \tag{3}$$

where

$$a = \langle a \rangle^f + a', \quad \langle a \rangle^f = \frac{1}{V_f} \int_{V_f} a \, \mathrm{d}V, \tag{4a, b}$$

in general denotes the intrinsic averaged value of a over the volume space V_f occupied by the fluid within a local control volume V, where the subscript f stands for the fluid phase. Moreover, the interfacial heat transfer coefficient is defined by

$$h_f \equiv \frac{\dfrac{1}{V}\displaystyle\int_{A_{int}} k_f \frac{\partial T}{\partial x_j} n_j \, \mathrm{d}A}{(\langle T \rangle^s - \langle T \rangle^f)}, \tag{5}$$

where n_j is the unit vector normal to the interface pointing from the fluid side to the solid side. The net heat transfer between the fluid and the solid is given by $h_f a_f(\langle T \rangle^f - \langle T \rangle^s)$ where a_f is the specific interfacial area (i.e. interfacial area per unit volume).

This single set of the volume-averaged governing equations may be applied to the entire calculation domain within the complex heat transfer equipment consisting of small-scale elements, as we specify the spatial distributions of the porosity $\phi = V_f/V$ and permeability, such that the clear fluid flow region without small-scale obstructions may be treated as a special case by setting $\phi = 1$ and infinitely large permeability. However, in order to use these macroscopic equations for such numerical analyses, we must close the equations by modelling the flow resistance (i.e. K_{ij} and b_{ij}) associated with individual subscale solid elements and also the heat transfer rate (i.e. h_f) between the flowing fluid and the subscale elements, in terms of the local velocity vector and relevant geometrical parameters.

The microscopic numerical results obtained at a pore scale can be processed to extract the macroscopic hydrodynamic and thermal characteristics in terms of the volume-averaged quantities. A great deal of effort has been directed towards this endeavour (Kuwahara, Nakayama & Koyama 1994; Nakayama & Kuwahara 1999, 2000; De Lemos & Pedras 2001; Pedras & De Lemos 2001). The unknown model parameters including the interfacial heat transfer coefficient, permeability and Forchheimer constants were determined by carrying out exhaustive numerical experiments using a periodic array of square rods and then integrating these microscopic results over a unit porous structure (Nakayama & Kuwahara 1999; Kuwahara, Shirota & Nakayama 2001). Nakayama *et al.* (2002*b*) proposed a bundle of rectangular cylinders to describe anisotropic porous media, and determined the permeability tensor, inertial (i.e. Forchheimer) tensor and interfacial heat transfer coefficient as functions of the macroscopic velocity vector and structural parameters. All these previous investigations, however, are limited to the cases of the crossflows over two-dimensional structures. In reality, all manmade elements such as those in plate fin heat exchangers are of a three-dimensional nature. Naturally, the macroscopic velocity vector is not always perpendicular to the axis of the cylinder. Thus, the three-dimensional yaw effects on the permeability tensor, inertial tensor and interfacial heat transfer coefficient must be elucidated beforehand, in order to design such heat transfer elements and systems.

Our literature survey has revealed that no explicit periodic thermal boundary conditions have been reported for the case of three-periodic boundaries in a three-dimensional space. In this paper, it will be shown that, under macroscopically uniform flow, the three-dimensional governing equations reduce to quasi-three-dimensional forms, in which all derivatives associated with the axis of the cylinder can be either eliminated or replaced by other determinable expressions. Thus, only two-dimensional storage is required for the dependent variables. This quasi-three-dimensional numerical calculation procedure will be exploited to investigate the

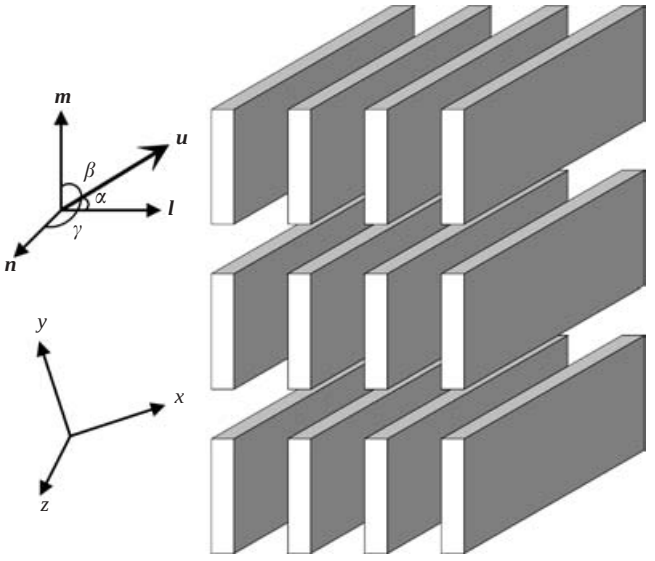

FIGURE 1. Coordinate system.

three-dimensional effects on the permeability tensor, inertial tensor and directional interfacial heat transfer coefficient, which are required to close the proposed set of macroscopic governing equations, and thus, expected to serve as fundamental data for designing certain heat transfer elements.

In what follows, we shall first present the macroscopic velocity and temperature fields prevailing in the bank of cylinder, which leads us to the appropriate periodic boundary conditions for the calculations of microscopic velocity and temperature fields within a unit element, and eventually to the quasi-three-dimensional calculation procedure. Using this inexpensive and yet efficient calculation procedure, the important macroscopic parameters, such as permeability tensor, inertial tensor and interfacial heat transfer coefficient will be determined by integrating the microscopic results over a unit structure for various sets of the porosity, degree of anisotropy, Reynolds number and macroscopic flow direction, such that the yaw effects on these macroscopic parameters will be elucidated. Upon correlating these macroscopic results, a useful set of explicit expressions will be established for the permeability tensor, Forchheimer tensor and directional interfacial heat transfer coefficient, so as to characterize flow and heat transfer through a bank of cylinders. No explicit correlations of this kind to estimate the drag and heat transfer from the bank of cylinders in yaw have ever been reported elsewhere.

2. Macroscopic velocity and temperature fields

Let us consider a macroscopically uniform flow through a bank of infinitely long cylinders, as shown in figure 1. The cross-section of the cylinder may be rectangular (as in a fin) or circular (as in a tube). The cylinder rows of the bank may be either aligned (as in the figure) or staggered. Such bank arrangements are relevant to various industrial applications such as cooling from extended fins and steam generation in tubular (and shell-and-tube) heat exchangers.

In most bank configurations, flow and heat transfer conditions stabilize for a cylinder beyond the first few rows such that the flow and heat transfer characteristics

under periodically fully developed conditions are of particular interest. Thus, we shall consider an infinitely large bank to investigate the periodically fully developed velocity and temperature fields. The bank structure may be regarded as an anisotropic porous medium, in which three principal axes ($\boldsymbol{l}, \boldsymbol{m}, \boldsymbol{n}$) are mutually orthogonal. Referring to these axes, the macroscopic velocity vector may be presented by

$$\langle \boldsymbol{u} \rangle = |\langle \boldsymbol{u} \rangle| (\cos\alpha \boldsymbol{l} + \cos\beta \boldsymbol{m} + \cos\gamma \boldsymbol{n}), \tag{6}$$

where the Darcian (apparent) velocity $\langle \boldsymbol{u} \rangle (= \phi \langle \boldsymbol{u} \rangle^f)$ is used in place of the intrinsic velocity $\langle \boldsymbol{u} \rangle^f$. Note that the directional cosines of the macroscopic flow satisfy the obvious relationship, namely,

$$\cos^2\alpha + \cos^2\beta + \cos^2\gamma = 1. \tag{7a}$$

This relation may be rewritten equivalently using the projected angle α' (i.e. crossflow angle) as

$$\cos\alpha = \sin\gamma \cos\alpha', \quad \cos\beta = \sin\gamma \sin\alpha'. \tag{7b}$$

Under the macroscopically uniform velocity as given by (6), the volume averaged momentum equation, (2), reduces to

$$-\frac{\partial \langle p \rangle^f}{\partial x_i} = \left(\mu_f K_{f_{ij}}^{-1} + \rho_f b_{f_{ij}} |\langle \boldsymbol{u} \rangle|\right) \langle u_j \rangle, \tag{8}$$

where

$$\langle u_k \rangle \langle u_k \rangle = |\langle \boldsymbol{u} \rangle|^2. \tag{9}$$

Thus, the macroscopic momentum equation leads to the Forchheimer extended Darcy's law (Forchheimer 1901), generalized for the case of anisotropic porous media.

We shall assume that the outer surfaces of the cylinders are maintained at a constant temperature. Then, the microscopic temperature field, when averaged spatially within a local control volume, should lead to the macroscopic temperature field whose gradient aligns with the macroscopic velocity vector in the s direction, such that the volume averaged energy equation (3), under the macroscopically uniform velocity field, reduces to

$$\rho_f c_{p_f} |\langle \boldsymbol{u} \rangle| \frac{\mathrm{d} \langle T \rangle^f}{\mathrm{d}s} = -h_f a_f (\langle T \rangle^f - \langle T \rangle^s), \tag{10}$$

where

$$\mathrm{d}s = (\cos\alpha \boldsymbol{l} + \cos\beta \boldsymbol{m} + \cos\gamma \boldsymbol{n}) \cdot (\boldsymbol{i}\, \mathrm{d}x + \boldsymbol{j}\, \mathrm{d}y + \boldsymbol{k}\, \mathrm{d}z), \tag{11}$$

where $\langle T \rangle^f$ and $\langle T \rangle^s$ denote the intrinsic averaged temperature of fluid and that of the cylinders, respectively. Since the surface temperature of the cylinders $\langle T \rangle^s$ is constant, this equation naturally yields

$$\langle T \rangle^f - \langle T \rangle^s = (\langle T \rangle^f - \langle T \rangle^s)_{ref} \exp\left(-\frac{a_f h_f}{\rho_f c_{p_f} |\langle \boldsymbol{u} \rangle|}(s - s_{ref})\right). \tag{12}$$

Note that the interfacial heat transfer coefficient h_f is expected to be constant for the periodically fully developed heat and fluid flow (Kuwahara *et al.* 2001), as in the case of fully developed flow in a tube or channel with isothermal walls. This macroscopic temperature distribution leads us to find the appropriate periodic boundary conditions for the calculations at a pore scale, as will be described in the following chapter.

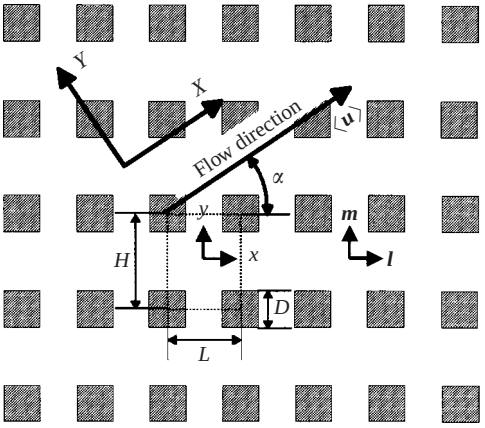

FIGURE 2. Numerical model.

3. Governing equations and periodic boundary conditions

The microscopic governing equations for the fluid are given as follows:

$$\nabla \cdot \boldsymbol{u} = 0, \tag{13}$$

$$\rho_f (\nabla \cdot \boldsymbol{u}) \boldsymbol{u} = -\nabla p + \mu_f \nabla^2 \boldsymbol{u}, \tag{14}$$

$$\rho_f c_{p_f} \nabla \cdot (\boldsymbol{u} T) = k_f \nabla^2 T. \tag{15}$$

Consider a periodically fully developed flow through a periodic structure, as shown in figure 2. Upon aligning Cartesian coordinates (x, y, z) with the principal axes of the structure and taking their origin in the centre of the structural unit ($-L/2 \leqslant x \leqslant L/2$, $-H/2 \leqslant y \leqslant H/2$, $-M/2 \leqslant z \leqslant M/2$), the boundary, compatibility and periodic constraints for the microscopic velocity field are given by

on the solid walls:

$$\boldsymbol{u} = \boldsymbol{0}, \tag{16a}$$

$$T = T_w (= \langle T \rangle^s), \tag{16b}$$

on the periodic boundaries:

$$\boldsymbol{u}|_{x=-L/2} = \boldsymbol{u}|_{x=L/2}, \tag{17a}$$

$$\boldsymbol{u}|_{y=-H/2} = \boldsymbol{u}|_{y=H/2}, \tag{17b}$$

$$\boldsymbol{u}|_{z=-M/2} = \boldsymbol{u}|_{z=M/2}. \tag{17c}$$

In order to establish the macroscopically uniform flow as given by (6), the following mass flow rate constraints must be satisfied:

$$\int_{-M/2}^{M/2} \int_{-H/2}^{H/2} u \, \mathrm{d}y \, \mathrm{d}z \bigg|_{x=-L/2} = \int_{-M/2}^{M/2} \int_{-H/2}^{H/2} u \, \mathrm{d}y \, \mathrm{d}z \bigg|_{x=L/2} = HM \cos\alpha \langle |\boldsymbol{u}| \rangle, \tag{18a}$$

$$\int_{-M/2}^{M/2} \int_{-L/2}^{L/2} v \, \mathrm{d}x \, \mathrm{d}z \bigg|_{y=-H/2} = \int_{-M/2}^{M/2} \int_{-L/2}^{L/2} v \, \mathrm{d}x \, \mathrm{d}z \bigg|_{y=H/2} = LM \cos\beta \langle |\boldsymbol{u}| \rangle, \tag{18b}$$

$$\int_{-H/2}^{H/2} \int_{-L/2}^{L/2} w \, \mathrm{d}x \, \mathrm{d}y \bigg|_{z=-M/2} = \int_{-H/2}^{H/2} \int_{-L/2}^{L/2} w \, \mathrm{d}y \, \mathrm{d}x \bigg|_{z=M/2} = LH \cos\gamma \langle |\boldsymbol{u}| \rangle. \tag{18c}$$

Thus, at the periodically fully developed stage, the velocity distribution on one plane of the structural unit must be identical to that on its adjacent plane.

On the other hand, the temperature profile on one plane is not identical but similar to that on the adjacent plane, since the rods maintained at constant temperature heat (or cool) the fluid as it passes over them. Kuwahara *et al.* (2001) have uniquely determined the periodic thermal boundary conditions, which lead to the macroscopic temperature distribution as given by (12) for the case of the two-dimensional (cross) flows over the isothermal square cylinders. These periodic thermal boundary conditions may easily be extended for the case of three-dimensional periodic convective flow. Thus, we find that, for the macroscopic temperature distribution given by (12) to prevail, the corresponding microscopic temperature field must satisfy the following similarity conditions:

$$(T - T_w)|_{x=L/2} = \tau^{L\cos\alpha/(L\cos\alpha+H\cos\beta+M\cos\gamma)}\,(T - T_w)|_{x=-L/2}\,, \tag{19a}$$

$$(T - T_w)|_{y=H/2} = \tau^{H\cos\beta/(L\cos\alpha+H\cos\beta+M\cos\gamma)}\,(T - T_w)|_{y=-H/2}\,, \tag{19b}$$

$$(T - T_w)|_{z=M/2} = \tau^{M\cos\gamma/(L\cos\alpha+H\cos\beta+M\cos\gamma)}\,(T - T_w)|_{z=-M/2}\,, \tag{19c}$$

where

$$\tau = \frac{(T - T_w)|_{x=L/2,y=H/2,z=M/2}}{(T - T_w)|_{x=-L/2,y=-H/2,z=-M/2}}. \tag{20}$$

Our literature survey has revealed that no explicit periodic thermal boundary conditions (such as given by (19)) have been reported for the case of three-periodic boundaries in a three-dimensional space.

4. Quasi-three-dimensional numerical model

As a numerical model for small-scale heat transfer elements, we consider a macroscopically uniform flow through a bank of square cylinders (or tubes) placed in an anisotropic fashion (see figure 2). All square cylinders, which may be regarded as heat sinks (or sources), are maintained at a constant temperature T_w, which is lower (or higher) than the temperature of the flowing fluid.

Since the cylinders are infinitely long, the governing equations reduce to a quasi-three-dimensional form, in consideration of the limiting case, namely, $M \to 0$:

$$\frac{\partial u}{\partial x} + \frac{\partial v}{\partial y} = 0, \tag{21}$$

$$\frac{\partial}{\partial x}\left(u^2 - \nu_f \frac{\partial u}{\partial x}\right) + \frac{\partial}{\partial y}\left(vu - \nu_f \frac{\partial u}{\partial y}\right) = -\frac{1}{\rho_f}\frac{\partial p}{\partial x}, \tag{22a}$$

$$\frac{\partial}{\partial x}\left(uv - \nu_f \frac{\partial v}{\partial x}\right) + \frac{\partial}{\partial y}\left(v^2 - \nu_f \frac{\partial v}{\partial y}\right) = -\frac{1}{\rho_f}\frac{\partial p}{\partial y}, \tag{22b}$$

$$\frac{\partial}{\partial x}\left(uw - \nu_f \frac{\partial w}{\partial x}\right) + \frac{\partial}{\partial y}\left(vw - \nu_f \frac{\partial w}{\partial y}\right) = \frac{\nu_f}{A_{fluid}} \oint_{P_{int}} \frac{\partial w}{\partial n}\,\mathrm{d}P, \tag{23}$$

$$\frac{\partial}{\partial x}\left(uT - \frac{\nu_f}{Pr_f}\frac{\partial T}{\partial x}\right) + \frac{\partial}{\partial y}\left(vT - \frac{\nu_f}{Pr_f}\frac{\partial T}{\partial y}\right) = S_w, \tag{24}$$

where P is the coordinate along the wetted periphery, whereas n is the coordinate normal to P pointing inward from the peripheral wall to fluid side. A_{fluid} is the passage

area of the fluid, and

$$S_w = -\frac{\partial}{\partial z}\left(wT - \frac{\nu_f}{Pr_f}\frac{\partial T}{\partial z}\right)$$
$$= -\left(w - \frac{\nu_f}{Pr_f}\frac{\cos\gamma \ln(\tau)_{z=0}}{L\cos\alpha + H\cos\beta}\right)\frac{\cos\gamma \ln(\tau)_{z=0}(T - T_w)_{z=0}}{L\cos\alpha + H\cos\beta}, \tag{25}$$

since

$$\frac{\partial T}{\partial z} = (T - T_w)_{z=0}\lim_{M\to 0}\frac{\tau^{M\cos\gamma/(L\cos\alpha + H\cos\beta + M\cos\gamma)} - 1}{M}$$
$$= \frac{(T(x, y, 0) - T_w)\cos\gamma}{L\cos\alpha + H\cos\beta}\ln\left(\frac{(T - T_w)_{x=L/2, y=H/2, z=0}}{(T - T_w)_{x=-L/2, y=-H/2, z=0}}\right). \tag{26}$$

In this way, all derivatives associated with z can be eliminated. Thus, only two-dimensional storage is required to solve (21)–(24). (Note that both (23) and (24) may be treated as two-dimensional scalar transport equations.)

5. Numerical calculation procedure

Equations (21), (22*a*) and (22*b*) along with the boundary and constraint conditions given by (17*a*), (17*b*), (18*a*) and (18*b*) form a closed set of equations for determining u, v and p. Therefore, the velocity and pressure fields of u, v and p can be established independently of the remaining velocity component w. The velocity component w can be determined later, solving (23) using the resulting u, v and p solutions along with the mass flow constraint given by (18*c*). Having established the three-dimensional velocity field, the temperature field may readily be established, solving (24) along with (19*a*), (19*b*) and (25).

For this periodic structure, the representative elementary volume V of the unit can be taken as $L \times H$. Because of the periodicity of the model, only the unit as indicated by dashed lines in the figure may be taken as a calculation domain.

Computations may be made using the dimensionless equations based on the absolute value of the Darcian (apparent) velocity vector $|\langle \boldsymbol{u} \rangle|$, and the longitudinal centre-to-centre distance L as reference scales. For carrying out a series of numerical calculations, it may be convenient to use the Reynolds number based on L as $Re_L = |\langle \boldsymbol{u} \rangle| L/\nu_f$, which can readily be translated into the Reynolds number based on the size of the square rod D as follows:

$$Re_D = |\langle \boldsymbol{u} \rangle| D/\nu_f = \left((1 - \phi)\frac{H}{L}\right)^{1/2} Re_L, \tag{27}$$

where the porosity is given by

$$\phi = 1 - (D^2/HL). \tag{28}$$

In this study, the Reynolds number is varied from 10^{-2} to 6×10^3, as in the previous study for the crossflows (i.e. with $\gamma = \pi/2$). Here, both crossflow angle α' and yaw angle γ are varied from 0 to $\pi/2$ with an increment $\pi/36$ to cover all possible macroscopic flow directions in the three-dimensional space, such that entire solution surfaces may be constructed over the domain $0 \leqslant \alpha' \leqslant \pi/2$ and $0 \leqslant \gamma \leqslant \pi/2$. Moreover, the ratio H/L is set to 1, 3/2 and 2 to investigate the effects of the degree of the anisotropy, whereas the ratio D/L is fixed to 1/2 for all calculations.

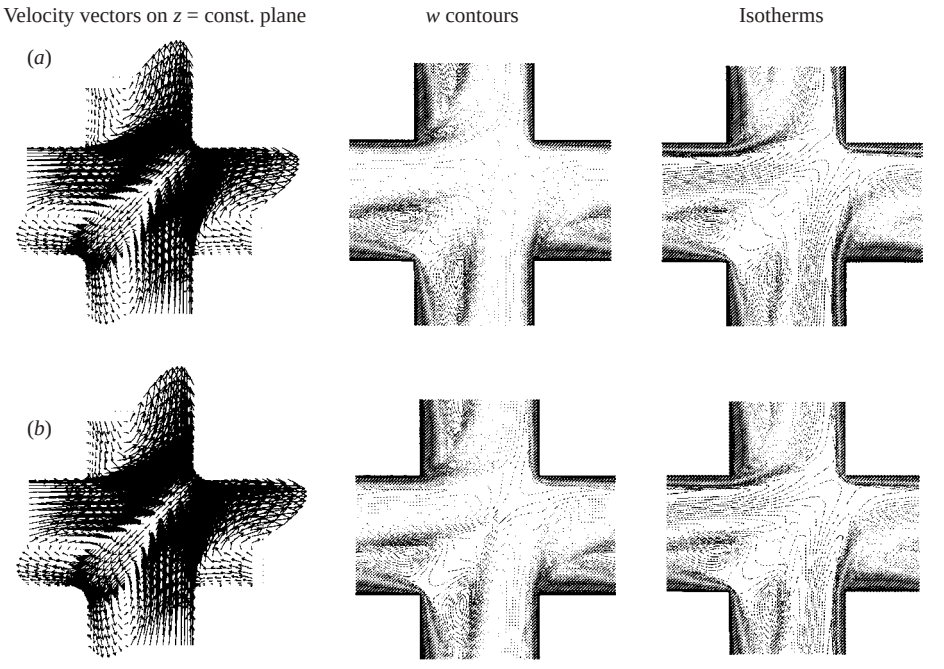

FIGURE 3. Comparison of two distinct three-dimensional calculation procedures ($H/L = 1$, $\alpha' = 45°$, $\gamma = 45°$, $Re_L = 600$, $Pr = 1$). (*a*) Results based on the full three-dimensional calculation procedure; (*b*) on the quasi-three-dimensional calculation procedure.

The governing equations (21), (22*a*) and (22*b*) subject to the foregoing boundary and compatibility conditions were solved numerically using the SIMPLE algorithm proposed by Patankar & Spalding (1972). As the u and v velocity fields were established, the remaining equations (23) and (24) were solved to find w and T. Convergence was measured in terms of the maximum change in each variable during an iteration. The maximum change allowed for the convergence check was set to 10^{-5}, as the variables are normalized by appropriate references. The hybrid scheme is adopted for the advection terms. Further details on this numerical procedure can be found in Patankar (1980) and Nakayama, Chow & Sharma (1983). All computations have been carried out for one structural unit $L \times H$ using non-uniform grid arrangements with 91×91, after comparing the results against those obtained with 181×181 for some selected cases, and confirming that the results are independent of the grid system. All computations were performed using the computer system at Shizuoka University Computer Center.

In order to check the validity of the present quasi-three-dimensional calculation procedure, full three-dimensional calculations have been carried out using (13)–(15) for some selected cases. In figure 3, the resulting velocity and temperature fields for the case of $H/L = 1$, $\alpha' = 45°$, $\gamma = 45°$, $Re_L = 600$ and $Pr = 1$ are compared with those based on the quasi-three-dimensional calculation procedure. Excellent agreement between the two sets of results can be seen, which verifies the accuracy and efficiency of the proposed quasi-three-dimensional calculation procedure. The CPU time required for convergence using the full three-dimensional calculation was roughly 3 h, which is 6 times more than that using the quasi-three-dimensional calculation. This proves the effectiveness of the quasi-three-dimensional calculation procedure.

6. Determination of the permeability tensor

The gradient of the intrinsic average pressure may readily be evaluated using the microscopic results as

$$-\frac{\partial \langle p\rangle^f}{\partial s} = \frac{\cos\alpha}{L(H-D)}\int_{-(H-D)/2}^{(H-D)/2}\left(p|_{x=-L/2} - p|_{x=L/2}\right)\mathrm{d}y + \frac{\cos\beta}{H(L-D)}\int_{-(L-D)/2}^{(L-D)/2}\left(p|_{y=-H/2} - p|_{y=H/2}\right)\mathrm{d}y + \frac{\mu_f\cos\gamma}{(HL-D^2)}\oint_{P_f}\frac{\partial w}{\partial n}\,\mathrm{d}P. \quad (29)$$

When the velocity (i.e. Reynolds number) is low, the proposed model equation (8) reduces to Darcy's law as

$$-\frac{\partial \langle p\rangle^f}{\partial x_i} = \left(\mu_f K_{f_{ij}}^{-1} + \rho_f b_{f_{ij}}|\langle \boldsymbol{u}\rangle|\right)\langle u_j\rangle \cong \mu_f K_{f_{ij}}^{-1}\langle u_j\rangle. \quad (30)$$

For the orthotropic media, the permeability tensor may be modelled following Dullien (1979) as

$$K_{f_{ij}}^{-1} = (l_i l_j)/K_{f_1} + (m_i m_j)/K_{f_2} + (n_i n_j)/K_{f_3}, \quad (31)$$

such that

$$-\frac{\partial \langle p\rangle^f}{\partial x_i} \cong \mu_f K_{f_{ij}}^{-1}\langle u_j\rangle = \left(\frac{\cos\alpha}{K_{f_1}}l_i + \frac{\cos\beta}{K_{f_2}}m_i + \frac{\cos\gamma}{K_{f_3}}n_i\right)|\langle \boldsymbol{u}\rangle| \quad (32)$$

where

$$\cos\alpha = \frac{l_j\langle u_j\rangle}{|\langle \boldsymbol{u}\rangle|}, \quad \cos\beta = \frac{m_j\langle u_j\rangle}{|\langle \boldsymbol{n}\rangle|}, \quad \cos\gamma = \frac{n_j\langle u_j\rangle}{|\langle \boldsymbol{u}\rangle|}. \quad (33)$$

Thus, the directional permeability measured along the macroscopic flow direction s is given by

$$\frac{1}{K_{f_n}} = \frac{\cos^2\alpha}{K_{f_1}} + \frac{\cos^2\beta}{K_{f_2}} + \frac{\cos^2\gamma}{K_{f_3}}, \quad (34)$$

such that

$$-\frac{\partial \langle p\rangle^f}{\partial s} = \frac{\mu_f}{K_{f_n}}|\langle \boldsymbol{u}\rangle|, \quad (35)$$

or, in dimensionless form, as

$$-\frac{\partial \langle p\rangle^f}{\partial s}\frac{L^2}{\mu_f|\langle \boldsymbol{u}\rangle|} = \frac{L^2}{K_{f_n}}. \quad (36)$$

Thus, the directional permeability K_{f_n} may readily be determined by reading the intercept of the ordinate variable, as we plot $-(\partial\langle p\rangle^f/\partial s)(L^2/\mu_f|\langle \boldsymbol{u}\rangle|)$ against Re_L, as done in the previous study on the crossflow case (Nakayama *et al.* 2002*a*, *b*). The solution surfaces of the directional permeability are constructed using the numerical values and presented in terms of L^2/K_{f_n} against the projected angle α' and the yaw angle γ for the cases of $H/L = 1$ and $3/2$ in figure 4(*a*). The solution surface changes drastically as the ratio H/L departs from unity. Note that the effect of the projected angle α' on the directional permeability is totally absent for the arrangement $H/L = 1$.

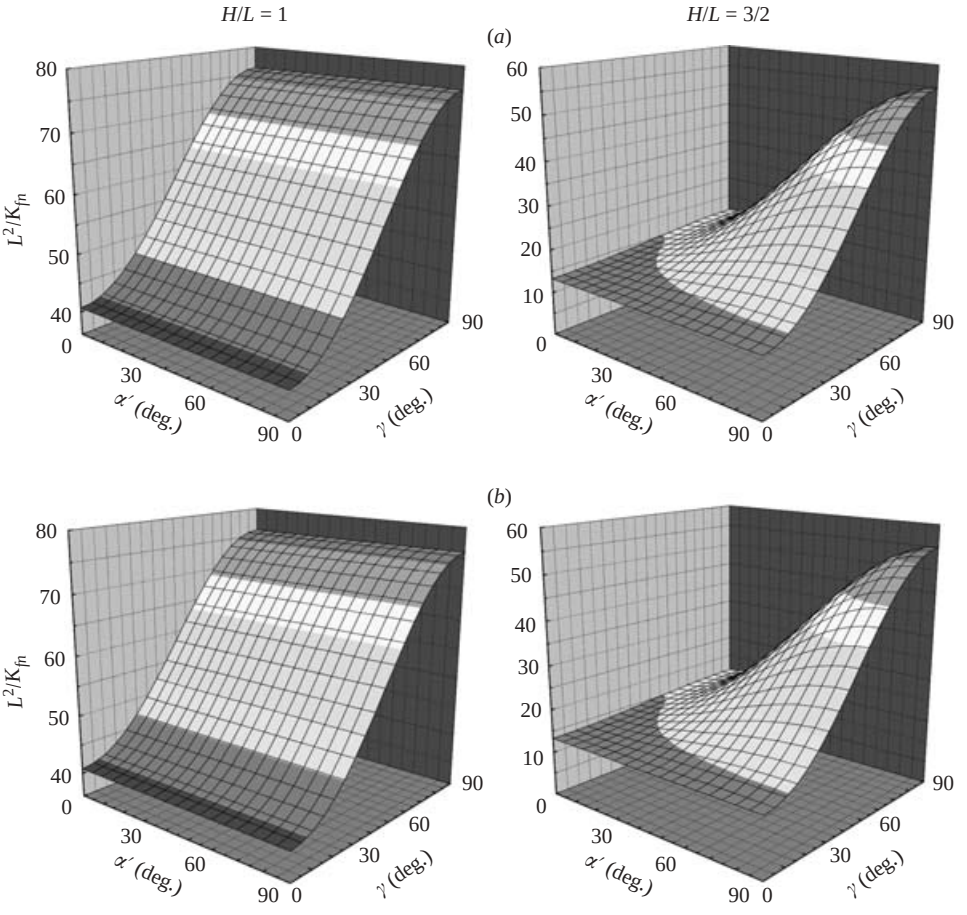

FIGURE 4. Solution surfaces for directional permeability. (*a*) Numerical experiments. (*b*) Correlations.

$H/L(\phi)$	L^2/K_{f_1}	L^2/K_{f_2}	L^2/K_{f_3}	$b_{f_1}L$	$b_{f_2}L$	$bb_{f_1}L$
1 (0.750)	76	76	41	0.2	0.2	8.2
3/2 (0.833)	16	55	13	0.1	0.6	3.2
2 (0.875)	7	42	6	0.05	0.8	1.2

TABLE 1. Coefficients for macroscopic pressure gradient.

The coefficients K_{f_1}, K_{f_2} and K_{f_3} in the proposed expression (34) may be determined by fitting the numerical results against the solution surfaces based on (34). Such solution surfaces generated by the proposed equation (34) are presented in figure 4(*b*) for comparison. The numerical values of K_{f_1}, K_{f_2} and K_{f_3} determined in this manner are given in table 1.The validity of the proposed equation (34) with the values given in table 1 can be examined further by plotting L^2/K_{f_n} as shown in figure 5 for the case of $\gamma = \pi/2$, where the fluid flows perpendicularly to the rods. It is seen that the numerical results closely follow the curves generated from (34).

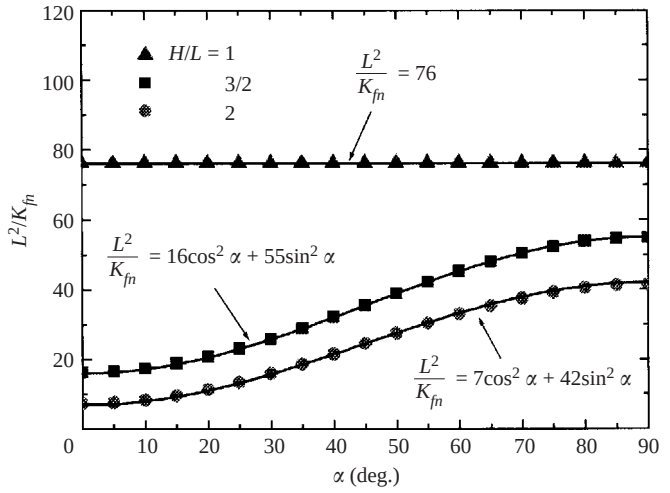

FIGURE 5. Directional permeability at $\gamma = \pi/2$.

7. Determination of the Forchheimer tensor

When the velocity (i.e. Reynolds number) is sufficiently high, the Forchheimer term describing the form drag predominates over the Darcy term such that

$$-\frac{\partial \langle p \rangle^f}{\partial x_i} = \left(\mu_f K_{f_{ij}}^{-1} + \rho_f b_{f_{ij}} |\langle \boldsymbol{u} \rangle|\right) \langle u_j \rangle \cong \rho_f b_{f_{ij}} |\langle \boldsymbol{u} \rangle| \langle u_j \rangle . \tag{37}$$

Usually, the principal axes of the permeability tensor $K_{f_{ij}}^{-1}$ do not coincide with those of the Forchheimer tensor $b_{f_{ij}}$. For the orthotropic media in consideration, however, the tensors $b_{f_{ij}}$ should be symmetric and they must also satisfy the following symmetric conditions:

$$\left.\frac{\partial b_{f_n}}{\partial \alpha}\right|_{\alpha=0,\pi/2} = \left.\frac{\partial b_{f_n}}{\partial \beta}\right|_{\beta=0,\pi/2} = \left.\frac{\partial b_{f_n}}{\partial \gamma}\right|_{\gamma=0,\pi/2} = 0, \tag{38}$$

where

$$b_{f_n} \equiv b_{f_{ij}} \frac{\langle u_i \rangle \langle u_j \rangle}{|\langle \boldsymbol{u} \rangle|^2} \tag{39}$$

is the directional Forchheimer coefficient measured along the macroscopic flow direction s. One of the simplest functions that satisfies these conditions may be:

$$\begin{aligned} b_{f_{ij}} = {} & b_{f_1}(l_i l_j) + b_{f_2}(m_i m_j) + b_{f_3}(n_i n_j) + b b_{f_1} \cos\alpha \cos\beta((l_i m_j) + (l_j m_i)) \\ & + b b_{f_2} \cos\beta \cos\gamma((m_i n_j) + (m_j n_i)) + b b_{f_3} \cos\gamma \cos\alpha((n_i l_j) + (n_j l_i)), \end{aligned} \tag{40}$$

which results in

$$\begin{aligned} b_{f_n} = {} & b_{f_1} \cos^2\alpha + b_{f_2} \cos^2\beta + b_{f_3} \cos^2\gamma + 2 b b_{f_1} \cos^2\alpha \cos^2\beta \\ & + 2 b b_{f_2} \cos^2\beta \cos^2\gamma + 2 b b_{f_3} \cos^2\gamma \cos^2\alpha, \end{aligned} \tag{41}$$

such that

$$-\frac{\partial \langle p \rangle^f}{\partial s} = \frac{\mu_f}{K_{f_n}} |\langle \boldsymbol{u} \rangle| + \rho_f b_{f_n} |\langle \boldsymbol{u} \rangle|^2 \tag{42}$$

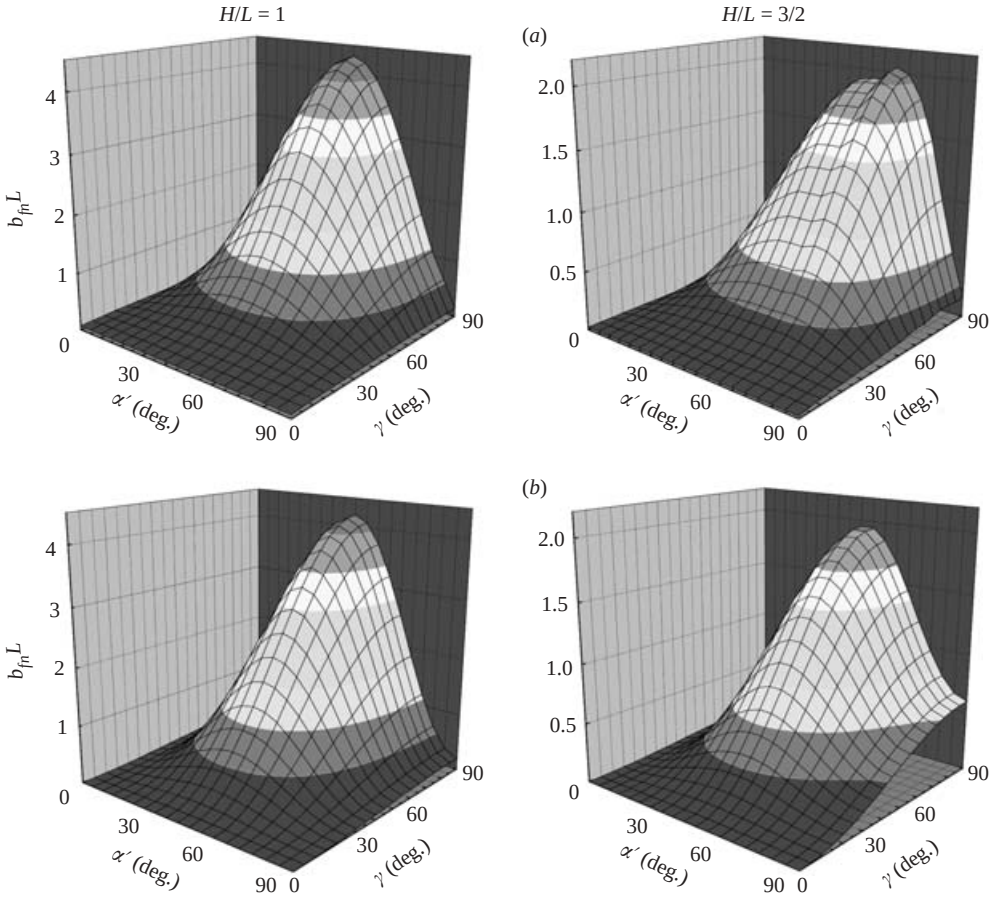

FIGURE 6. Solution surfaces for directional Forchheimer coefficient. (*a*) Numerical experiments. (*b*) Correlations.

or, in dimensionless form, as

$$-\frac{\partial \langle p \rangle^f}{\partial s}\frac{L}{\rho_f |\langle \boldsymbol{u} \rangle|^2} = \frac{L^2}{K_{f_n} Re_L} + b_{f_n} L. \tag{43}$$

Plotting the results of macroscopic pressure gradient in terms of $-(\partial \langle p \rangle^f / \partial s) \times (L/\rho_f |\langle \boldsymbol{u} \rangle|^2)$ and reading the horizontal asymptotes, we can readily determine the directional Forchheimer constant.

The numerical values of the directional Forchheimer constant for the cases of $H/L = 1$ and $3/2$ are shown in terms the solution surfaces of $b_{f_n} L$ in figure 6(*a*). These figures clearly show that, for fixed γ, the directional Forchheimer constant attains its peak around $\alpha' = \pi/2$, while, for fixed α', it decreases monotonically from $\gamma = \pi/2$ to 0.

From this observation, we find that the coefficients and bb_{f_1} is non-zero while b_{f_3}, bb_{f_2} and bb_{f_3} in (41) should vanish for the bank of cylinders, such that

$$\begin{aligned} b_{f_n} &= b_{f_1} \cos^2 \alpha + b_{f_2} \cos^2 \beta + 2bb_{f_1} \cos^2 \alpha \cos^2 \beta \\ &= \left(b_{f_1} \cos^2 \alpha' + b_{f_2} \sin^2 \alpha' + 2bb_{f_1} \cos^2 \alpha' \sin^2 \alpha' \sin^2 \gamma \right) \sin^2 \gamma. \end{aligned} \tag{44}$$

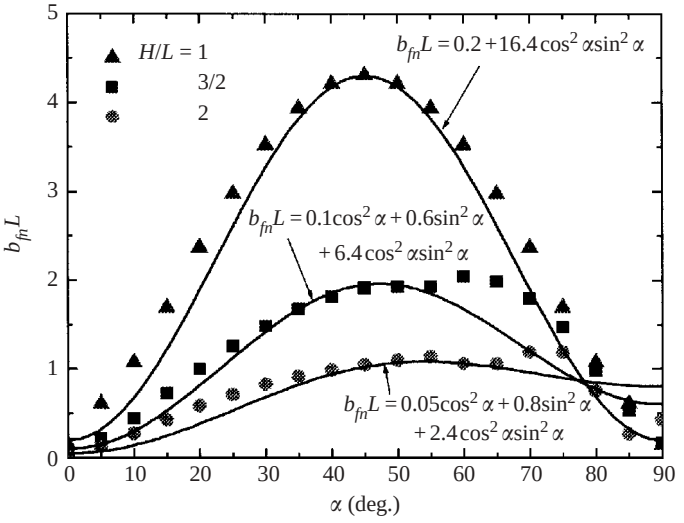

FIGURE 7. Directional Forchheimer coefficient at $\gamma = \pi/2$.

The corresponding $b_{f_n}L$ surfaces based on the proposed expression (44) with the values of b_{f_1} b_{f_2} and bb_{f_1} as given in table 1 are presented in figure 6(*b*) for comparison. Furthermore, the numerical results of the directional Forchheimer constant obtained with $\gamma = \pi/2$ for $H/L = 1$, 3/2 and 2 are presented in figure 7 as a function of the crossflow angle $\alpha(=\alpha')$. In the same figure, the solid curves generated from the proposed equation (44) are presented to elucidate the validity of the proposed expression. Note that, for this case of $\gamma = \pi/2$, the foregoing equation reduces to

$$b_{f_n} = b_{f_1}\cos^2\alpha + b_{f_2}\sin^2\alpha + 2bb_{f_1}\cos^2\alpha\sin^2\alpha. \tag{45}$$

The numerical results for the cases $H/L = 3/2$ and 2 show two consecutive peaks, whereas the model equation (45) yields only one peak (the first peak). The second peak appears when the macroscopic flow angle α reaches roughly $\tan^{-1}(H/L)$. Note that, for the case of $H/L = 1$, this second peak coincides with the first one. Unfortunately, the model equation is incapable of describing the second peak.

Zukauskas (1982) assembled the experimental data for the fully developed pressure drop across the tube banks in both inline-square and staggered-triangle arrangements, and presented a chart for the Euler number (i.e. the dimensionless macroscopic pressure gradient). His inline-square arrangement corresponds to the present arrangement with $\alpha = 0$, $\gamma = \pi/2$ and $L/D = 2$. However, it is noted that, in reality, the macroscopic flow direction rarely coincides with the principal axes, since even small disturbances at a sufficiently high Reynolds number make the flow deviate from the axis. Thus, it is understood that the chart provided by Zukauskas gives only the average level of the pressure drop within a range of small α (say $0° < \alpha < 5°$). The dimensionless macroscopic pressure gradient $-(\partial\langle p\rangle^f/\partial s)(L/\rho_f|\langle \boldsymbol{u}\rangle|^2)$ for the case of $\gamma = \pi/2$ and $L/D = 2$ is plotted against Re_L in Figure 8, where the curves generated from the model equation (43) with the numerical values taken from table 1 and figure 7 (note that $b_{f_n}L = 0.2$ and 0.6, for $\alpha = 0°$ and 5°, respectively) are drawn together with the empirical chart provided by Zukauskas for the inline-square arrangement. The agreement between these curves appears fairly good.

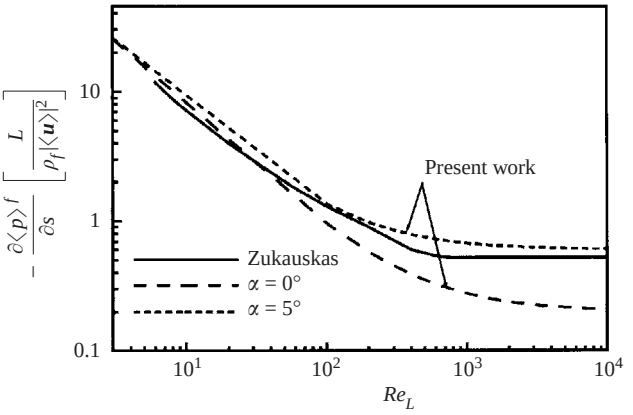

FIGURE 8. Dimensionless macroscopic pressure gradient.

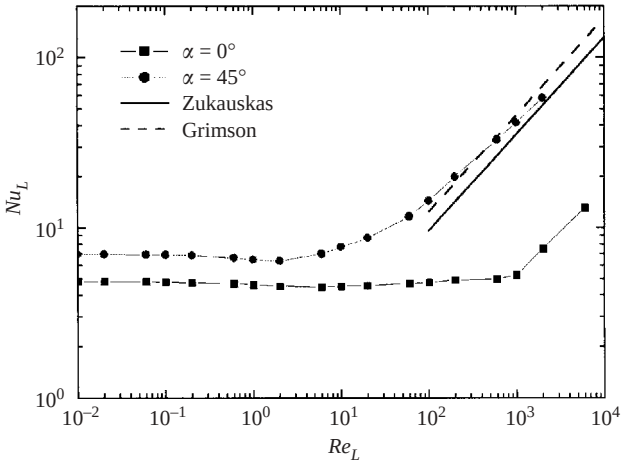

FIGURE 9. Effect of Reynolds number on directional Nusselt number ($Pr = 1$).

8. Determination of interfacial heat transfer coefficient

According to Kuwahara *et al.* (2001), the interfacial heat transfer coefficient as defined by equation (5) may be obtained by substituting the microscopic temperature results into the following equation:

$$h_f \equiv \frac{\dfrac{1}{V}\displaystyle\int_{A_{int}} k_f \nabla T \cdot \mathrm{d}\boldsymbol{A}}{(\langle T\rangle^s - \langle T\rangle^f)} = \frac{\dfrac{1}{A_{fluid}}\displaystyle\oint_{P_{int}} \left(-k_f \frac{\partial T}{\partial n}\right) \mathrm{d}P}{(\langle T\rangle^s - \langle T\rangle^f)}, \tag{46}$$

where A_{int} is the total interface between the fluid and solid, while $\mathrm{d}\boldsymbol{A}$ is its vector element pointing outward from the fluid side to solid side. In figure 9, the heat transfer results obtained at $\alpha = 0$ and $\pi/4$ for the crossflows (i.e. $\gamma = \pi/2$) are presented in terms of the interfacial Nusselt number $Nu_L = h_f L/k_f$ against the Reynolds-number Re_L. The figure suggests that the lower- and higher Reynolds-number data follow two distinct limiting lines for the case of non-zero α, namely, $\alpha = \pi/4$. The lower-Reynolds number data stay constant for the given array and flow angle, whereas the high Reynolds-number data vary in proportion to $Re_L^{0.6}$.

Another series of computations changing the Prandtl number, conducted following Kuwahara *et al.* (2001), revealed that the exponents associated with the Reynolds and Prandtl numbers are the same as those Wakao & Kaguei (1982) observed by collecting and scrutinizing reliable experimental data on interfacial convective heat transfer coefficients in packed beds. The similarity, albeit the difference in the Reynolds-number dependence, between the Nusselt number Nu_L and the macroscopic pressure gradient as given by (42) is noteworthy, which prompts us to model the directional Nusselt number as follows:

$$Nu_L \equiv \frac{h_f L}{k} = c_f + d_f Re_L^{0.6} Pr_f^{1/3}. \tag{47}$$

The experimental correlation proposed by Zukauskas (1987) for the heat transfer from the circular tubes in staggered banks is compared with the present results obtained for the case of $\alpha = \pi/4$, $\gamma = \pi/2$ and $H/L = 1$. (Note $Nu_f \cong Nu_L/2$ and $Re_f \cong Re_L$ in (39) of Zukauskas since $D/L = 1/2$.) The present results follow closely along the experimental correlation of Zukauskas with increasing Reynolds number. Grimson (1937) carried out an exhaustive experiment to investigate heat transfer from tube rows of a bank in both staggered and aligned arrangements with respect to the direction of the macroscopic flow. His case, in which the ratio of the transverse pitch to tube diameter and that of the longitudinal pitch to tube diameter are 3 and 1.5, respectively, gives a configuration close to the present orthogonal configuration with $\alpha = \pi/4$, $\gamma = \pi/2$ and $H/L = 1$. Thus, the experimental correlation established by Grimson for the case is also presented in the figure, which agrees very well with the present numerical results. These correlations are believed to hold for a comparatively wide Reynolds number range, covering from a predominantly laminar flow regime to turbulent flow regime.

Following a procedure similar to that adopted for determining the directional permeability, the coefficient $c_f \equiv Nu_L|_{Re_L \to 0}$ for each macroscopic flow angle is evaluated and plotted in terms of the solution surfaces in figures 10(*a*), using the low-Reynolds-number data. It is noted that the effect of the projected angle α' on the interfacial heat transfer coefficient is totally absent for the arrangement $H/L = 1$.

The similarity between the solution surfaces of c_f and those of L^2/K_{f_n} is obvious, which leads us to introduce a functional form as follows:

$$c_f = \left(c_{f_1}^{n_c} \cos^2\alpha + c_{f_2}^{n_c} \cos^2\beta + c_{f_3}^{n_c} \cos^2\gamma\right)^{1/n_c}, \tag{48}$$

such that c_f reduces to c_{f_1}, c_{f_2} and c_{f_3} for $\alpha = 0$, $\beta = 0$ and $\gamma = 0$, respectively, as it should.

Careful examination of the numerical results over the whole domain within $0 \leqslant \alpha' \leqslant \pi/2$ and $0 \leqslant \gamma \leqslant \pi/2$ suggests that n_c is close to minus one, which leads us to a harmonic mean expression as

$$\frac{1}{c_f} = \frac{\cos^2\alpha}{c_{f_1}} + \frac{\cos^2\beta}{c_{f_2}} + \frac{\cos^2\gamma}{c_{f_3}}. \tag{49}$$

The values of c_{f_1}, c_{f_2} and c_{f_3} listed in table 2 have been determined by fitting the numerical results against the foregoing equation. The resulting surfaces based on the proposed expression (49) are presented in figure 10(*b*) for their comparison with the surfaces based on the numerical experiments shown in figure 10(*a*). Furthermore, figure 11 shows the numerical results of c_f obtained at $\gamma = \pi/2$ for the three distinct arrangements, namely, $H/L = 1$, $3/2$ and 2. The solid curves in the figure are

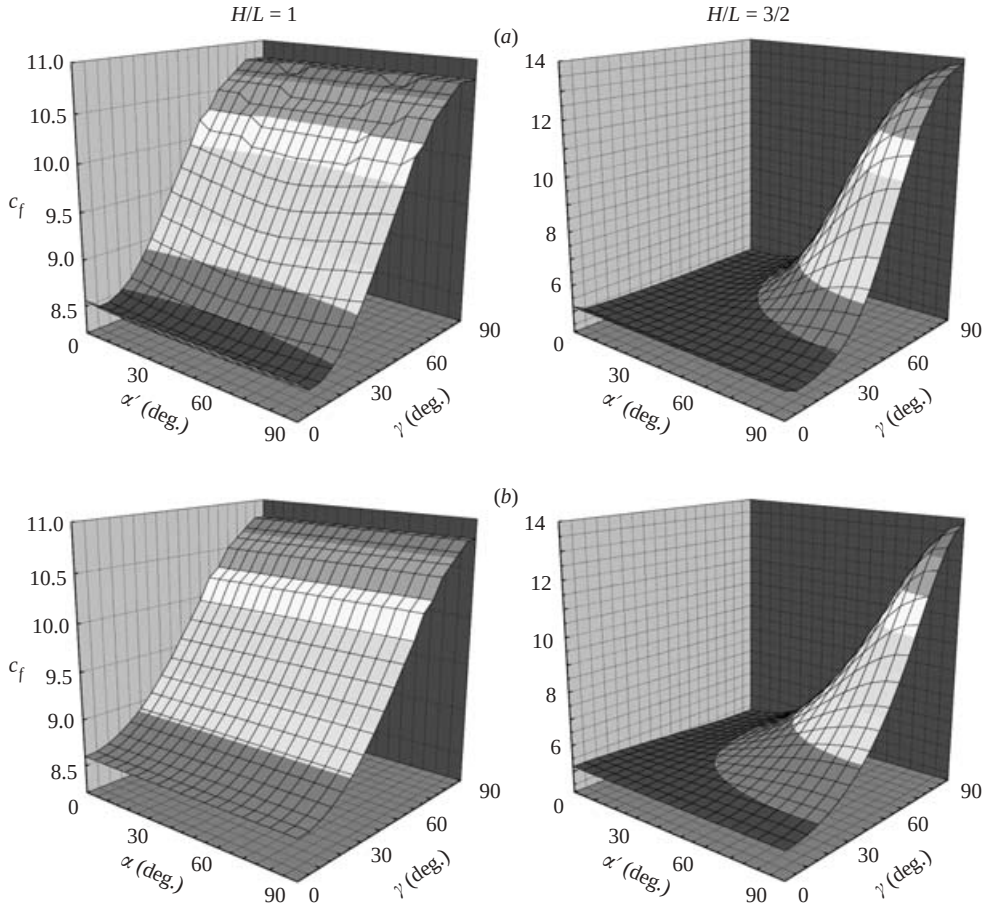

FIGURE 10. Solution surfaces for directional heat transfer coefficient at small Reynolds number. (*a*) Numerical experiments. (*b*) Correlations.

$H/L(\phi)$	c_{f_1}	c_{f_2}	c_{f_3}	n_c	$d_{f_1} = d_{f_2}$	n_d
1 (0.750)	11	11	8.6	−1.0	0.90	4.5
3/2 (0.833)	4.8	14	5.2	−1.0	0.77	4.5
2 (0.875)	3.2	16	3.6	−1.0	0.67	4.5

TABLE 2. Coefficients for directional Nusselt number.

generated from the proposed equation (49) with the values of c_{f_1} and c_{f_2} as given in table 2.

The second coefficient d_f may be determined using the data $Nu_L/Re_L^{0.6}Pr_f^{1/3}$ in the high-Reynolds-number range. The resulting solution surfaces of d_f are presented in figure 12 for $H/L = 1$ and 3/2. Unlike the Forchheimer coefficient b_{f_n}, the coefficient d_f stays roughly constant for a fixed yaw angle γ.

Somewhat more careful observation on the solution surfaces reveals that the coefficient d_f drops abruptly as the projected angle α' reaches close to either 0 or $\pi/2$ (in which the fluid flows along the principal axis of the structure). However, as

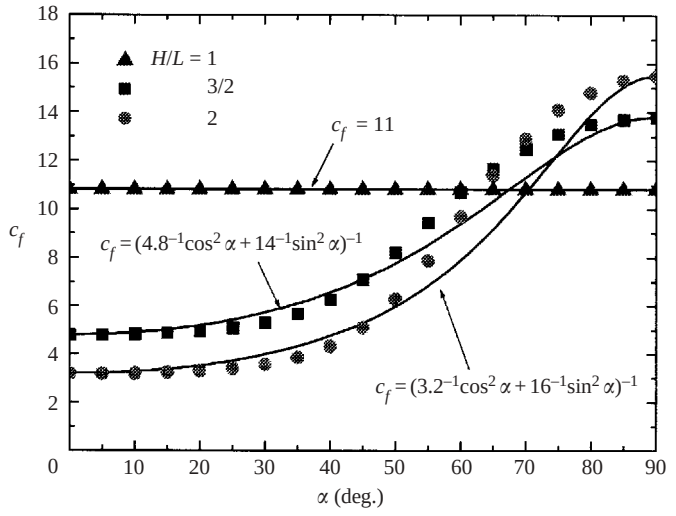

FIGURE 11. Effect of the crossflow angle α on the coefficient c_f at $\gamma = \pi/2$.

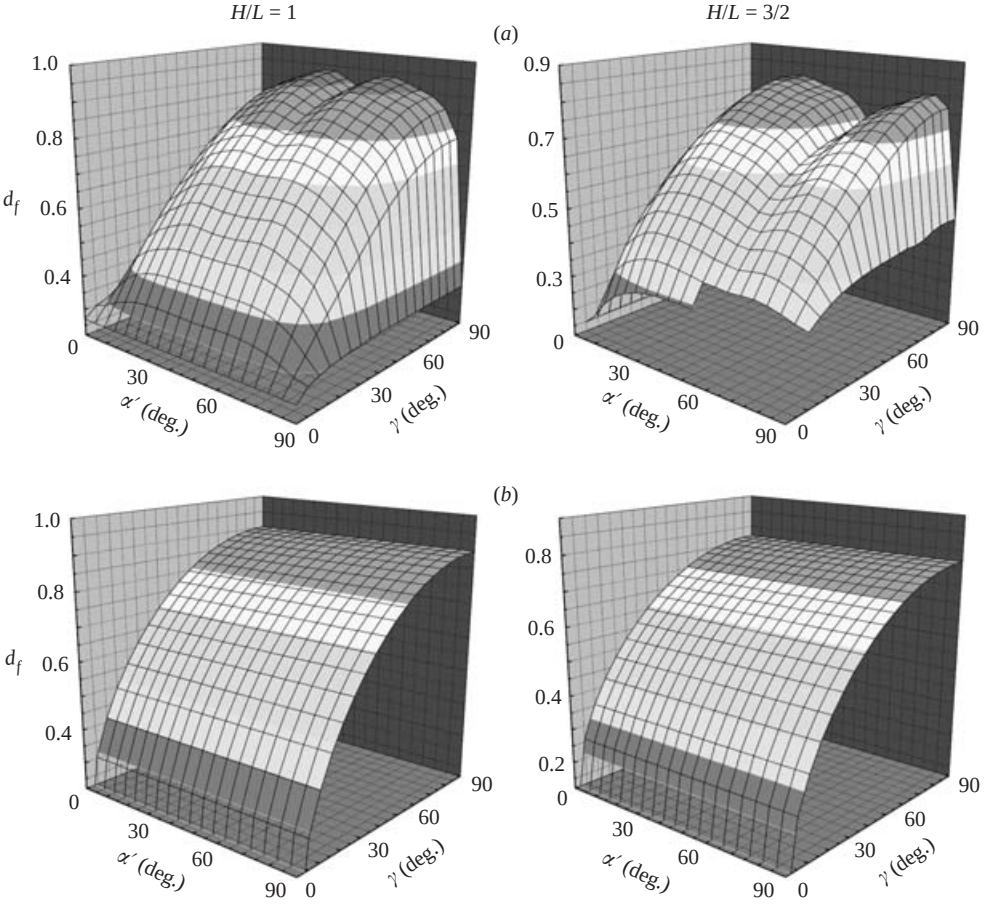

FIGURE 12. Solution surfaces for directional heat transfer coefficient at large Reynolds number. (*a*) Numerical experiments. (*b*) Correlations.

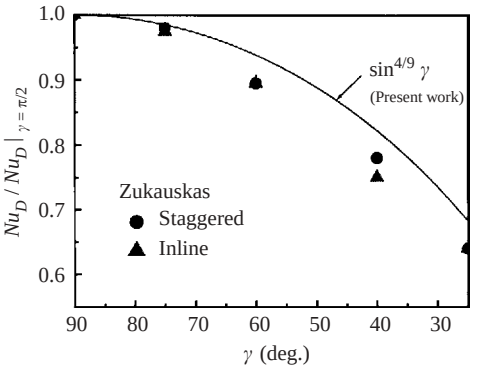

FIGURE 13. Effect of the yaw angle γ on the interfacial Nusselt number.

already pointed out, it is quite unlikely to have the macroscopic flow align perfectly with the principal axes. Thus, we may assume that d_f is the function of the yaw angle γ alone, namely, $d_f = d_f(\gamma)$. It is interesting to note that $d_f = d_f(\gamma)$ is consistent with the idea of the effective velocity $u_{eff} = |\langle \boldsymbol{u} \rangle| \sin\gamma$ used in hot-wire anemometry. Thus, we may model d_f as

$$d_f = \left(d_{f_1}^{n_d} \sin^2\gamma + d_{f_3}^{n_d} \cos^2\gamma\right)^{1/n_d} \tag{50}$$

A careful observation on the solution surfaces leads us to $d_{f_3} \cong 0$, and also reveals the values of d_{f_1} and n_d as given in table 2. Thus, we propose the following expression:

$$Nu_L = \left(c_{f_1}^{n_c} \cos^2\alpha + c_{f_2}^{n_c} \cos^2\beta + c_{f_3}^{n_c} \cos^2\gamma\right)^{1/n_c} + d_{f_1} \sin^{2/n_d}\gamma \, Re_L^{0.6} Pr_f^{1/3} \tag{51a}$$

or

$$Nu_D = \tfrac{1}{2}\left(c_{f_1}^{n_c} \cos^2\alpha + c_{f_2}^{n_c} \cos^2\beta + c_{f_3}^{n_c} \cos^2\gamma\right)^{1/n_c} + \frac{d_{f_1}}{2^{0.4}} \sin^{2/n_d}\gamma \, Re_D^{0.6} Pr_f^{1/3}. \tag{51b}$$

Note that the exponents $n_c = -1$ and $n_d = 9/2$ irrespective of the value of H/L, while the coefficients $c_{f_1}, c_{f_2}, c_{f_3}$ and d_{f_1} depend on that particular geometrical configuration.

Zukauskas (1982) investigated the effect of the yaw angle on the interfacial heat transfer rate. He varied the yaw angle γ for both staggered and aligned arrangements, and compared the corresponding heat transfer rates for the same Reynolds number. He pointed out that the data when normalized by the value obtained at $\gamma = \pi/2$ for all staggered and inline arrangements, namely, $Nu_D/Nu_D|_{\gamma=\pi/2}$, can be approximated by a single curve irrespective of the Reynolds number. His data for both staggered and inline arrangements are plotted in figure 13 together with the expression based on the model equation (51*b*), namely,

$$\frac{Nu_D}{Nu_D|_{\gamma=\pi/2}} \cong \sin^{2/n_d}\gamma = \sin^{4/9}\gamma \tag{52}$$

for the case of sufficiently high Reynolds number. The agreement between the experimental data and the curve based on (52) is fairly good, which indicates the validity of the model equation (51*b*). It should also be noted that the staggered arrangement corresponds to the case of $\alpha' = \pi/4$ while the inline arrangement corresponds to the case in which α' is close to zero (but $\alpha' \neq 0$ since the macroscopic flow direction never coincides with the principal axis of the structure). Thus, these experimental data substantiate our finding based on the numerical experiment, namely,

that the multiplicative constant for the interfacial Nusselt number d_f stays virtually constant (irrespective of α') for a fixed yaw angle, as illustrated by the solution surfaces in figure 12.

9. Conclusions

A quasi-three-dimensional calculation procedure has been proposed to investigate three-dimensional heat and fluid flow through a bank of cylinders in yaw, which represents a numerical model for manmade structures such as plate fin heat exchangers. Only one structural unit was taken as a calculation domain, noting the periodicity of the structure. This inexpensive and yet efficient numerical calculation procedure based on one structural unit along with periodic boundary conditions was exploited to conduct extensive three-dimensional calculations for a number of sets of the porosity, degree of anisotropy, Reynolds number, Prandtl number and macroscopic flow direction.The numerical results, thus obtained at the pore level, were integrated over a structural unit to determine the permeability tensor, Forchheimer tensor and directional interfacial heat transfer coefficient, so as to elucidate the effects of yaw angle on these macroscopic flow and heat transfer characteristics. Upon examing these numerical experimental data, a useful set of explicit expressions for the permeability tensor, Forchheimer tensor and directional interfacial heat transfer coefficient have been establised for the first time, such that we can easily evaluate the pressure drop and heat transfer rate from the bank of cylinders in yaw. The systematic modelling procedure proposed in this study can be used to conduct subscale modellings of manmade structures required in the possible applications of a volume averaging theory to investigate flow and heat transfer within complex heat and fluid flow equipment consisting of small elements.

REFERENCES

Bergelin, O. P., Brown, G. A. & Doberstein, S. C. 1952 Heat transfer and fluid friction during viscous flow across banks of tubes. IV. A study of the transition zone between viscous and turbulent flow. *Trans. ASME* **74**, 953–960.

Bergelin, O. P., Brown, G. A., Hull, H. L. & Sullivan, F. W. 1950 Heat transfer and fluid friction during viscous flow across banks of tubes. III. A study of tube spacing and tube size. *Trans. ASME* **72**, pp. 881–888.

Cheng, P. 1978 Heat transfer in geothermal systems. *Adv. Heat Transfer* 14, 1–105.

De Lemos, M. J. S. & Pedras, M. H. J. 2001 Recent mathematical models for turbulent flow in saturated rigid porous media. *Trans. ASME* I: *J. Fluids Engng* **123**, 935–940.

Dullien, F. A. L. 1979 *Porous Media: Fluid Transport and Pore Structure*. Academic.

Forchheimer, P. H. 1901 Wasserbewegung durch Boden. *Z. Ver. Dtsch. Ing.* **45**, 1782–1788.

Grimson, E. D. 1937 Correlation and utilization of new data on flow resistance and heat transfer for crossflow of gases over tube banks. *Trans. ASME* **59**, 583–594.

Grimson, E. D. 1938 Heat transfer and flow resistance of gases over tube banks. *Trans. ASME* **58**, 381–392.

Hubbert, M. K. 1956 Darcy's law and field equations of the flow of underground fluids. *AIME Petrol. Trans.* **207**, 222–239.

Kays, W. M. & London, A. L. 1984 *Compact Heat Exchangers*, 3rd edn. McGraw-Hill.

Kuwahara, F., Nakayama, A. & Koyama, H. 1994 Numerical modeling of heat and fluid flow in a porous medium. *Proc. 10th Intl Heat Transfer Conf.* vol. 5, pp. 309–314.

Kuwahara, F., Shirota, M. & Nakayama, A. 2001 A numerical study of interfacial convective heat transfer coefficient in two-energy equation model for convection in porous media. *Intl J. Heat Mass Transfer* **44**, 1153–1159.

Nakayama, A. 1995 *PC-Aided Numerical Heat Transfer and Convective Flow*. CRC Press, Boca Raton.

Nakayama, A., Chow, W. L. & Sharma, D. 1983 Calculation of fully developed turbulent flows of ducts of arbitrary cross-section. *J. Fluid Mech.* **128**, 199–217.

Nakayama, A. & Kuwahara, F. 1999 A macroscopic turbulence model for flow in a porous medium. *J. Fluids Engng* **121**, 427–433.

Nakayama, A. & Kuwahara, F. 2000 Numerical modeling of convective heat transfer in porous media using microscopic structures. In *Handbook of Porous Media* (ed. K. Vafai), pp. 441–488, Marcel Dekker.

Nakayama, A., Kuwahara, F., Naoki, A. & Xu, G. 2001 A three-energy equation model based on a volume averaging theory for analyzing complex heat and fluid flow in heat exchangers. *Proc. Intl Conf. Energy Conversion and Application, Wuhan, China (ICECA'2001)*, pp. 506–512.

Nakayama, A., Kuwahara, F., Naoki, A. & Xu, G. 2002*a* A volume averaging theory and its sub-control-volume model for analyzing heat and fluid flow within complex heat transfer equipment. *Proc. 12th Intl Heat Transfer Conf.* pp. 851–856.

Nakayama, A., Kuwahara, F., Umemoto, T. & Hayashi, T. 2002*b* Heat and fluid flow within an anisotropic porous medium. *J. Heat Transfer* **124**, 746–753.

Nakayama, A., Kuwahara, F. & Xu, G. 2001 A two-energy Equation model in porous media. *Intl J. Heat Mass Transfer* **44**, 4375–4379.

Omohundro, G. A., Bergelin, O. P. & Colburn, A. P. 1949 Heat transfer and fluid friction during viscous flow across banks of tubes. *Trans. ASME* **71**, 583–594.

Patankar, S. V. 1980 *Numerical Heat Transfer and Fluid Flow*. Hemisphere.

Patankar, S. V. & Spalding, D. B. 1972 A calculation procedure for heat, mass and momentum transfer in three-dimensional parabolic flows. *Intl J. Heat Mass Transfer* **15**, 1787–1806.

Pedras, M. H. J. & De Lemos, M. J. S. 2001 On the mathematical description and simulation of turbulent flow in a porous medium formed by an array of elliptic rods. *Trans. ASME* I: *J. Fluids Engng* **123**, 941–947.

Quintard, M. & Whitaker, S. 1993 One and two equation models for transient diffusion in two-phase systems. *Adv. Heat Transfer* **23**, 269–464.

Shah, R. K. & London, A. L. 1978 Laminar forced convection in ducts. *Adv. Heat Transfer, Suppl.* 1.

Slattery, J. C. 1967 Flow of viscoelastic fluids through porous media. *AIChE J.* **13**, 1066–1071.

Vafai, K. & Tien, C. L. 1981 Boundary and inertia effects on flow and heat transfer in porous media. *Intl J. Heat Mass Transfer* **24**, 195–203.

Wakao, N. & Kaguei, S. 1982 *Heat and Mass Transfer in Packed Beds*, pp. 243–295. Gorden and Breach.

Whitaker, S. 1967 Diffusion and dispersion in porous media. *AIChE J.* **13**, 420–427.

Zukauskas, A. 1982 *Konvektivnyi Perenos v Teploobmennikakh* (Convective Transfer in Heat Exchangers), p. 472. Nauka, Moscow.

Zukauskas, A. 1987 Heat transfer from tubes in crossflow. *Adv. Heat Transfer* **18**, 87–159.